RESEARCH PAPER

An explicit finite volume element method for solving characteristic level set equation on triangular grids

Sutthisak Phongthanapanich · Pramote Dechaumphai

Abstract Level set methods are widely used for predicting evolutions of complex free surface topologies, such as the crystal and crack growth, bubbles and droplets deformation, spilling and breaking waves, and two-phase flow phenomena. This paper presents a characteristic level set equation which is derived from the two-dimensional level set equation by using the characteristic-based scheme. An explicit finite volume element method is developed to discretize the equation on triangular grids. Several examples are presented to demonstrate the performance of the proposed method for calculating interface evolutions in time. The proposed level set method is also coupled with the Navier–Stokes equations for two-phase immiscible incompressible flow analysis with surface tension. The Rayleigh–Taylor instability problem is used to test and evaluate the effectiveness of the proposed scheme.

Keywords Characteristic level set equation · Finite volume element method · Explicit method · Triangular grid · Two-phase incompressible flow

1 Introduction

Computer simulation for interface motion problems by using

S. Phongthanapanich (✉)
Department of Mechanical Engineering Technology,
College of Industrial Technology,
King Mongkut's University of Technology North Bangkok,
Bangkok 10800, Thailand
e-mail: sutthisakp@kmutnb.ac.th

P. Dechaumphai
Mechanical Engineering Department,
Chulalongkorn University,
Bangkok 10330, Thailand

the level set principle was firstly introduced by Osher and Sethian [1]. It is not easy to solve these problems because a flow near the interface often has strong vortical components due to the related sharp gradients of the flow properties. To predict the flow phenomena accurately, the interface needs to be tracked precisely in both time and space. The interface normal vectors and curvatures are also needed to be approximate by a highly accurate numerical scheme in order to model the interface precisely [2]. The level set methods have gained popularity mainly due to their simplicity. Applications of the level set methods for moving boundaries and interfaces problems exist in many fields such as the crystal and crack growth, bubbles and droplets deformation, spilling and breaking waves, multiphase and multifluid flows, front propagations and fluid-structural interactions [3–7]. In general, the interface is represented by a zero level contour of a signed distance function. It is desirable to maintain the level set function, ϕ, as a signed distance function during the interface evolution for accurate interface capturing. Calculation of the interface normal vector and curvature from the level set method is straightforward but may not be necessarily accurate [8,9].

During the past decade, many researchers have introduced several high-order accurate numerical schemes which are based on the finite difference, finite element, and finite volume methods to discretize the level set equation. For examples, Fedkiw [10] proposed a numerical method for modeling a multimaterial flow where a domain is decomposed into the separate Eulerian and Lagrangian subdomains. The level set function is defined at every Eulerian grid node while ϕ is defined analytically at each Lagrangian interface node. The third-order essentially non-oscillatory local Lax-Friedrichs (ENO-LLF) and total variation diminishing (TVD) Runge–Kutta (RK) schemes were used to achieve a high-order accurate solution. Huang and Zhang [11] used a level set method to simulate a cavitation bubble. The Marker and Cell (MAC) projection and control volume method was

employed to improve the velocity and pressure solutions of the second-order ENO procedure to overcome the instability caused by the non-linear convection term. A level set method for solving the vaporizing two-phase flow problem, where the fifth-order weighted essentially non-oscillatory (WENO5) scheme is used to discretize the convective term, was studied by Tanguy et al.[12]. The Petrov–Galerkin finite element method was also used to discretize the level set equation to achieve high-order accurate solutions on unstructured meshes [13]. The level set method incorporated with the extended finite element method (XFEM) was employed to simulate the crack propagation behavior in a solid [5] where two level set functions were used to represent the open boundaries. The second-order finite volume method was applied to solve a two-phase flow problem through a conservative level set method [9]. The second-order TVD upwind method coupled with the second-order Runge–Kutta scheme was used to approximate a level set equation. In many of these mentioned methods, an intermediate step was added at the end of each time step to ensure that the interface remains constant. Recently, a high-resolution flux-based finite volume method has been introduced to approximate the level set equation on unstructured grids [14,15]. In these papers, the results are relatively good without applying any reinitialization technique to recover the numerical signed distance function.

The major disadvantage of the level set method is such that it can not provide a mass conservative property. For two-phase flow analysis, the interface given by a contour should be moved at the correct interface velocity. But the contour does not necessary remain a distance function, thus it can result in an irregular interface field. To heal this problem, many reinitialization techniques have been proposed in the past [8,10]. These techniques are numerical tools for healing (not for fixing) the distorted and stretched level set field. However, the reinitialization should be avoided as much as possible because they lead to the loss of mass and movement of the contour [13]. Many level set methods apply the second-order TVD-RK or the 4th-order RK time stepping schemes to arrive at the time accurate solution at the next time step. The applications need two and four computation cycles, to determine the flux terms. More computational time and computer memory are thus required. Additional numerical dissipations are also included in the process. These schemes are thus not very efficient for long time computation of many transient two-phase flow problems.

The objective of this work is to develop an explicit finite volume element method for solving the characteristic level set equation in a two-dimensional triangular domain. Recently, the combination of the conventional finite element and finite volume methods for solving fluid flow problems is of interest by many researchers [16,17]. However, the idea for using the finite volume scheme to discretize the characteristic level set equation has never been investigated. In this paper, the concept of the characteristic-based

scheme [18,19], for approximating the Lagrangian derivatives in time, is used to derive the characteristic level set equation. The advantage of the characteristic based split (CBS) scheme is that the approximate level set partial differential equation (PDE) gives a second-order accurate solution in time. An explicit finite volume method is employed to develop the discretized equations for the spatial domain. The advantage of the finite volume discretization is a conservative property. By combining these two methods together with a gradient reconstruction technique, a conservative second-order accurate solution in space and time with only one computation cycle is achieved. Theoretically, the conservative property implies that the proposed method may give a less mass loss than other methods. The gradients at cell faces for determining the curvature term are calculated by using the weighted-residual finite element technique. Performance of the proposed method is examined by analyzing two-dimensional examples. Results are compared with the known analytical solutions and/or those reported by other researchers. The presentation of this paper starts from explaining the theoretical formulation and corresponding characteristic-based scheme in Sect. 2. The finite volume discretization of the characteristic level set equation is presented in Sect. 3. Performance of the proposed method is evaluated in Sect. 4 by using four examples. Finally, in order to evaluate the efficiency of proposed method, the characteristic level set method is coupled with the Navier–Stokes equations for two-phase immiscible incompressible flow analysis with surface tension. The Rayleigh–Taylor instability problem is used to test and validate the performance of the proposed scheme.

2 Derivation of characteristic level set equation

The level set methods have been used widely to determine the evolution of interface problems. The methods are relatively simple and able to capture topological changes such as shrinking, merging and splitting easily without special treatments. For a two-dimensional domain, the advection-diffusion form of the level set function can be written as

$$\frac{\partial \phi}{\partial t} + \boldsymbol{V} \cdot \boldsymbol{\nabla} \phi - b\kappa |\boldsymbol{\nabla} \phi| = 0, \quad \text{in } \Omega \times T, \tag{1}$$

where $\phi = \phi(\boldsymbol{x}, t)$ defines the implicit interface by its zero level set which is chosen to be positive outside Ω^+, negative inside Ω^-, and zero on interface $(\partial \Omega_I)$, and $t \in (0, T)$ for $T < \infty$. The velocity field $\boldsymbol{V} = \boldsymbol{V}(\boldsymbol{x}, \nabla \phi(\boldsymbol{x}, t), t)$ can be defined in several ways depending on applications [3]. For example, the externally generated velocity field (advection) is $\boldsymbol{u}(\boldsymbol{x}, t)$, the velocity field for constant motion in the normal direction is $a\boldsymbol{\nabla}\phi/|\boldsymbol{\nabla}\phi|$ where b is a constant, and the curvature is $\kappa = \boldsymbol{\nabla} \cdot (\boldsymbol{\nabla}\phi/|\boldsymbol{\nabla}\phi|)$. The initial condition is defined for $\boldsymbol{x} \in \Omega$ with $\Omega \subset R^2$ and $\Omega = \Omega^+ \cup \Omega^- \cup \partial \Omega_I$ by $\phi(\boldsymbol{x}, 0) = \phi_0(\boldsymbol{x})$.

By following the procedure described in Refs.[18,19], Eq. (1) is semi-discretized along the characteristic line so

that it can be written in the form

$$\frac{1}{\Delta t}\left(\phi^{n+1}\big|_{\boldsymbol{x}} - \phi^{n}\big|_{\boldsymbol{x}-\Delta\boldsymbol{x}}\right)$$

$$= \frac{1}{2}\left[(b\kappa|\boldsymbol{\nabla}\phi|)^{n}\big|_{\boldsymbol{x}-\Delta\boldsymbol{x}} + (b\kappa|\boldsymbol{\nabla}\phi|)^{n+1}\big|_{\boldsymbol{x}}\right], \qquad (2)$$

where $\phi = \phi(\boldsymbol{x}',t)$ and $\boldsymbol{x}'$ is the path of the characteristic wave. The incremental time period Δt is from n to $n + 1$, and the incremental distance $\Delta\boldsymbol{x}$ is from $\boldsymbol{x} - \Delta\boldsymbol{x}$ to $\boldsymbol{x}$. The local Taylor's series expansion in space is applied to the second term on the left-hand side and to the right-hand side terms. The incremental distance $\Delta\boldsymbol{x}$ along the characteristic path is then approximated by $\Delta\boldsymbol{x} = \boldsymbol{V}^{n+1/2}\Delta t$, where $\boldsymbol{V}^{n+1/2}$ is the average velocity along the characteristic line at time $t = n + 1/2$ [19]. Equation (2) can then be written in a fully explicit form

$$\frac{1}{\Delta t}(\phi^{n+1} - \phi^{n}) = \Big[-\boldsymbol{V}\cdot\boldsymbol{\nabla}\phi + b\kappa|\boldsymbol{\nabla}\phi|$$

$$+\frac{\Delta t}{2}(\boldsymbol{\nabla}\phi\boldsymbol{V}\cdot\boldsymbol{\nabla}\boldsymbol{V} + \boldsymbol{V}\boldsymbol{V}\cdot\boldsymbol{\nabla}^{2}\phi)\Big]^{n}. \qquad (3)$$

By utilizing the vector identity

$$\boldsymbol{\nabla}\phi\boldsymbol{V}\cdot\boldsymbol{\nabla}\boldsymbol{V} + \boldsymbol{V}\boldsymbol{V}\cdot\boldsymbol{\nabla}^{2}\phi = \boldsymbol{V}\cdot\boldsymbol{\nabla}\boldsymbol{V}\cdot\boldsymbol{\nabla}\phi, \qquad (4)$$

the characteristic level set equation becomes

$$\frac{1}{\Delta t}(\phi^{n+1} - \phi^{n}) = \Big(-\boldsymbol{V}\cdot\boldsymbol{\nabla}\phi + b\kappa|\boldsymbol{\nabla}\phi| + \frac{\Delta t}{2}\boldsymbol{V}\cdot\boldsymbol{\nabla}\boldsymbol{V}\cdot\boldsymbol{\nabla}\phi\Big)^{n}. \quad (5)$$

Finally, Eq. (5) can be written preferably in the conservation form for applying the finite volume method as

$$\phi^{n+1} - \phi^{n} = -\Delta t[\boldsymbol{\nabla}\cdot(\boldsymbol{V}\phi) + \phi\boldsymbol{\nabla}\cdot\boldsymbol{V} - b\kappa|\boldsymbol{\nabla}\phi|]^{n}$$

$$+\frac{(\Delta t)^{2}}{2}[\boldsymbol{\nabla}\cdot(\boldsymbol{V}\boldsymbol{\nabla}\phi\cdot\boldsymbol{V}) - \boldsymbol{V}\cdot\boldsymbol{\nabla}\phi\boldsymbol{\nabla}\cdot\boldsymbol{V}]^{n}. \qquad (6)$$

3 Explicit discretization

The computational domain is first discretized into a collection of non-overlapping convex polygon control volumes $\Omega_i \in \Omega$, $i = 1, 2, \cdots, N$, that completely cover the domain such that $\Omega = \bigcup_{i=1}^{N}\Omega_i$, $\Omega_i \neq 0$, and $\Omega_i \cap \Omega_j = 0$ if $i \neq j$. Equation (6) is integrated over the control volume Ω_i to obtain

$$\int_{\Omega_i}(\phi^{n+1} - \phi^{n})\mathrm{d}\boldsymbol{x}$$

$$= \int_{\Omega_i} -\Delta t[\boldsymbol{\nabla}\cdot(\boldsymbol{V}\phi) + \phi\boldsymbol{\nabla}\cdot\boldsymbol{V} - b\kappa|\boldsymbol{\nabla}\phi|]^{n}\mathrm{d}\boldsymbol{x}$$

$$+ \int_{\Omega_i}\frac{(\Delta t)^{2}}{2}[\boldsymbol{\nabla}\cdot(\boldsymbol{V}\boldsymbol{\nabla}\phi\cdot\boldsymbol{V}) - \boldsymbol{V}\cdot\boldsymbol{\nabla}\phi\boldsymbol{\nabla}\cdot\boldsymbol{V}]^{n}\mathrm{d}\boldsymbol{x}. \quad (7)$$

The divergence theorem is applied to some spatial terms on the right-hand side of the equation to yield

$$\int_{\Omega_i}\phi(\boldsymbol{x}, t^{n+1})\mathrm{d}\boldsymbol{x}$$

$$= \int_{\Omega_i}\phi(\boldsymbol{x}, t^{n})\mathrm{d}\boldsymbol{x} - \Delta t\int_{\partial\Omega_i}\boldsymbol{n}_i(\nu)\cdot\{\boldsymbol{V}(\nu, t^{n})\phi(\nu, t^{n})$$

$$-b|\boldsymbol{\nabla}\phi(\boldsymbol{x}, t^{n})|[\boldsymbol{\nabla}\phi(\nu, t^{n})/|\boldsymbol{\nabla}\phi(\nu, t^{n})|]$$

$$-\frac{\Delta t}{2}\boldsymbol{V}(\nu, t^{n})\boldsymbol{\nabla}\phi(\boldsymbol{x}, t^{n})\cdot\boldsymbol{V}(\boldsymbol{x}, t^{n})\}\mathrm{d}\nu$$

$$+\Delta t\int_{\Omega_i}[\phi(\boldsymbol{x}, t^{n})\boldsymbol{\nabla}\cdot\boldsymbol{V}(\boldsymbol{x}, t^{n})$$

$$-\frac{\Delta t}{2}\boldsymbol{V}(\boldsymbol{x}, t^{n})\cdot\boldsymbol{\nabla}\phi(\boldsymbol{x}, t^{n})\boldsymbol{\nabla}\cdot\boldsymbol{V}(\boldsymbol{x}, t^{n})]\mathrm{d}\boldsymbol{x}, \qquad (8)$$

where $\boldsymbol{n}_i(\nu)$ is the unit outward normal vector of $\partial\Omega_i$. The approximation to the cell average of ϕ over Ω_i at time t^n and t^{n+1} is represented by [14]

$$\phi_i^{n+1} = \frac{1}{|\Omega_i|}\int_{\Omega_i}\phi(\boldsymbol{x}, t^{n+1})\mathrm{d}\boldsymbol{x},$$

$$\phi_i^{n} = \frac{1}{|\Omega_i|}\int_{\Omega_i}\phi(\boldsymbol{x}, t^{n})\mathrm{d}\boldsymbol{x}, \qquad (9)$$

where $|\Omega_i|$ is the measure of Ω_i. For any control volume, the flux integral over $\partial\Omega_i$ appearing on the right-hand side of Eq. (8) could be approximated by the summation of fluxes passing through all adjacent cell faces. Hence, by applying the midpoint quadrature integration rule to the second integration term on the right-hand side of Eq. (8), the flux integral over $\partial\Omega_i$ is

$$\int_{\partial\Omega_i}\boldsymbol{n}_i(\nu)\cdot\boldsymbol{V}(\nu, t^{n})\phi(\nu, t^{n})\mathrm{d}\nu = \sum_{j=1}^{3}|\Gamma_{ij}|\boldsymbol{n}_{ij}\cdot\boldsymbol{V}_{ij}^{n}\phi_{ij}^{n}, \qquad (10)$$

$$\int_{\partial\Omega_i}\boldsymbol{n}_i(\nu)\cdot b|\boldsymbol{\nabla}\phi(\boldsymbol{x}, t^{n})|[\boldsymbol{\nabla}\phi(\nu, t^{n})/|\boldsymbol{\nabla}\phi(\nu, t^{n})|]\mathrm{d}\nu$$

$$= b|\boldsymbol{\nabla}\phi_i^{n}|\sum_{j=1}^{3}|\Gamma_{ij}|\boldsymbol{n}_{ij}\cdot\frac{\boldsymbol{\nabla}\phi_{ij}^{n}}{|\boldsymbol{\nabla}\phi_{ij}^{n}|}, \qquad (11)$$

$$\int_{\partial\Omega_i}\boldsymbol{n}_i(\nu)\cdot\frac{\Delta t}{2}\boldsymbol{V}(\nu, t^{n})\boldsymbol{\nabla}\phi(\boldsymbol{x}, t^{n})\cdot\boldsymbol{V}(\boldsymbol{x}, t^{n})\mathrm{d}\nu$$

$$= \frac{\Delta t}{2}\boldsymbol{V}_i^{n}\cdot\boldsymbol{\nabla}\phi_i^{n}\sum_{j=1}^{3}|\Gamma_{ij}|\boldsymbol{n}_{ij}\cdot\boldsymbol{V}_{ij}^{n}. \qquad (12)$$

The term that appears in the third integration term on the right-hand side of Eq. (8), is approximated as the source terms by

$$\int_{\Omega_i}\phi(\boldsymbol{x}, t^{n})\boldsymbol{\nabla}\cdot\boldsymbol{V}(\boldsymbol{x}, t^{n})\mathrm{d}\boldsymbol{x} = \phi_i^{n}\sum_{j=1}^{3}|\Gamma_{ij}|\boldsymbol{n}_{ij}\cdot\boldsymbol{V}_{ij}^{n}, \qquad (13)$$

and

$$\int_{\Omega_i}\frac{\Delta t}{2}\boldsymbol{V}(\boldsymbol{x}, t^{n})\cdot\boldsymbol{\nabla}\phi(\boldsymbol{x}, t^{n})\boldsymbol{\nabla}\cdot\boldsymbol{V}(\boldsymbol{x}, t^{n})\mathrm{d}\boldsymbol{x}$$

$$= \frac{\Delta t}{2}\boldsymbol{V}_i^{n}\cdot\boldsymbol{\nabla}\phi_i^{n}\sum_{j=1}^{3}|\Gamma_{ij}|\boldsymbol{n}_{ij}\cdot\boldsymbol{V}_{ij}^{n}, \qquad (14)$$

where Γ_{ij} is the segment of boundary $\partial\Omega_i$ between two adjacent control volumes Ω_i and Ω_j, which is defined by

$$\partial \Omega_i = \bigcup_{j=1}^{3} \Gamma_{ij} \text{ and } \Gamma_{ij} = \partial \Omega_i \cap \partial \Omega_j.$$

By substituting Eqs. (9)–(14) into Eq. (8), a fully explicit formulation for solving a characteristic level set equation (1) is obtained in the form

$$\phi_i^{n+1} = \phi_i^n - \frac{\Delta t}{|\Omega_i|} \sum_{j=1}^{3} |\Gamma_{ij}| \boldsymbol{n}_{ij} \cdot \boldsymbol{V}_{ij}^n \left[\phi_{ij}^n - \frac{\Delta t}{2} (\boldsymbol{V}_i^n \cdot \boldsymbol{\nabla} \phi_i^n) \right]$$

$$+ \frac{\Delta t}{|\Omega_i|} b |\boldsymbol{\nabla} \phi_i^n| \sum_{j=1}^{3} |\Gamma_{ij}| \boldsymbol{n}_{ij} \cdot \frac{\boldsymbol{\nabla} \phi_{ij}^n}{|\boldsymbol{\nabla} \phi_{ij}^n|}$$

$$+ \frac{\Delta t}{|\Omega_i|} \left(\phi_i^n - \frac{\Delta t}{2} \boldsymbol{V}_i^n \cdot \boldsymbol{\nabla} \phi_i^n \right) \sum_{j=1}^{3} |\Gamma_{ij}| \boldsymbol{n}_{ij} \cdot \boldsymbol{V}_{ij}^n, \quad (15)$$

where the quantities at time t^n are $\phi_{ij}^n = \phi_{ij}(t^n)$, $\phi_i^n = \phi_i(t^n)$, $\boldsymbol{V}_{ij}^n = \boldsymbol{V}_{ij}(t^n)$, and $\boldsymbol{V}_i^n = \boldsymbol{V}_i(t^n)$.

The level set function ϕ_{ij}^n at cell face at the full time step t^n, is approximated by applying the Taylor's series expansion in space such that

$$\phi_{ij}^n = \phi_i^n + (\boldsymbol{x}_{ij} - \boldsymbol{x}_i) \cdot \boldsymbol{\nabla} \phi_i^n, \quad (16)$$

where $\boldsymbol{x}_i$ and $\boldsymbol{x}_{ij}$ are the cell centroid and the face centroid locations, respectively, as shown in Fig. 1. For the opposite direction of velocity, the values of ϕ_{ij}^n could be computed from Eq. (16) but by using the values from the neighboring control volumes according to the upwinding direction, e.g. $\phi_{ij}^n = \phi_j^n + (\boldsymbol{x}_{ij} - \boldsymbol{x}_j) \cdot \boldsymbol{\nabla} \phi_j^n$.
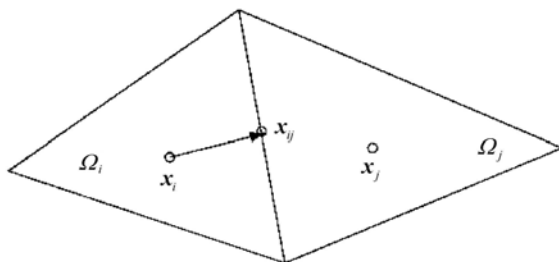

Fig. 1 Control volume and two adjacent cell faces

The gradient term for calculating the curvature, $\boldsymbol{\nabla} \phi_{ij}^n$, is approximated by the weighted residuals method [19]. Detailed explanation of the procedure for approximating this gradient term is described in Ref. [20] where it was applied to the unsteady reaction-diffusion problems.

4 Numerical test cases

In this section, performance of the proposed method is examined by using five examples. All examples are tested on uniform triangular grids. These examples are: (1) the rotation of an expanding circle; (2) the rotation of a slotted disk; (3) the reverse vortex test; (4) the motion by mean curvature of a star shape, and (5) the Rayleigh–Taylor instability

problem.

4.1 Rotation of an expanding circle

The first benchmark problem is a rotation of an expanding circle in a square domain of $\Omega = (-1, -1) \times (1, 1)$. This example has an analytical solution [9,14] so that the computed solution can be compared. Initially, the circle with a radius of 0.25 is centered at $(-0.4, 0.0)$ and is rotated with non divergence-free velocity field (advection velocity and interface normal velocity) given by

$$\boldsymbol{V} = (2\pi y, \ -2\pi x) + v_n \frac{\boldsymbol{\nabla} \phi}{|\boldsymbol{\nabla} \phi|}. \quad (17)$$

The divergence-free velocity field case where $v_n = 0$ is firstly examined. The final time is selected as 1.0, which is the time period required for one turn rotation. The exact solution at the final time is then described by a circle centered at $(-0.4, 0.0)$ with the radius of 0.35. To assess the order for convergence of the proposed method, the simulations are performed on the uniform grids S1–S4 consisting of 32×32 ($\Delta x = \Delta y = 1/32$), 64×64, 128×128, and 256×256, respectively. Example of the uniform triangular mesh S1 is shown in Fig. 2. The zero level contour plots of the exact and numerical solutions at the four different times of 0.25, 0.5, 0.75, and 1.0 are presented in Fig. 3. These figures show that the differences of the interface position between the exact and numerical solutions are quite small. They also show that the proposed method provides a smooth interface simulation even though the grid size is relatively coarsen (S1). The $\|L_{1,I}\|$ norm of numerical error is used to measure the difference of the numerical interface position from the exact solution which is defined by [21]

$$\|L_{1,I}\| = \frac{1}{L} \int_{\Omega} |H(\phi_{\text{num}}) - H(\phi_{\text{exa}})| d\boldsymbol{x}, \quad (18)$$

where L is the perimeter size of interface. The Heaviside function H is defined by $H(\phi) = 1$ if $\phi < 0$ and $H(\phi) = 0$ otherwise.
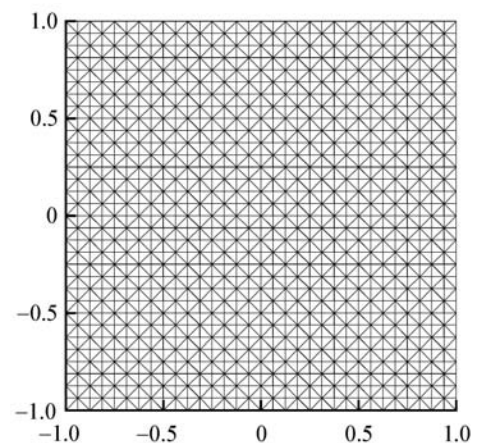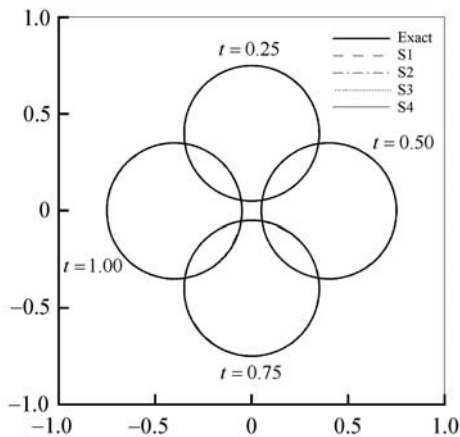


Fig. 2 Example of an uniform triangular grid S1

Fig. 3 Comparison of exact and numerical solutions on four grid sizes of Problem 4.1

The values of $\|L_{1,I}\|$ error norms and the rate of convergence are tabulated in Table 1. The table shows that the rate of convergence is approximately two. To assess the robustness and numerical accuracy for a longer time simulation, the problem is tested again by extending the final time to $t = 4.0$ (four turns rotation). The comparison of the interface positions between the exact and numerical solutions is shown in Fig. 4a. The figure indicates that all numerical solutions are good as compared to the exact solution, except the one obtained from the course mesh of grid S1. Figure 4b shows the level set function at $t = 4.0$ obtained from grid S4. It can be seen that the signed distance function (used as the initial level set function) is preserved during simulation without the application of a redistancing technique.

Table 1 $\|L_{1,I}\|$ error norms for different grid sizes of Problems 4.1, 4.2, 4.3

Problem 4.1		Problem 4.2		Problem 4.3	
Grid size	$\|L_{1,I}\|$	Grid size	$\|L_{1,I}\|$	Grid size	$\|L_{1,I}\|$
S1 (1/32)	$2.675\,6\times10^{-3}$	S2 (1/64)	$6.378\,3\times10^{-3}$	S2 (1/64)	$2.840\,0\times10^{-2}$
S2 (1/64)	$6.966\,4\times10^{-4}$	S3 (1/128)	1.9815×10^{-3}	S3 (1/128)	$1.275\,0\times10^{-2}$
S3 (1/128)	$1.509\,7\times10^{-4}$	S4 (1/256)	5.3012×10^{-4}	S4 (1/256)	$3.858\,0\times10^{-3}$
S4 (1/256)	$2.728\,4\times10^{-5}$	S5 (1/512)	$1.223\,3\times10^{-4}$	S5 (1/512)	$1.232\,8\times10^{-4}$
Convergence rate	2.21	Convergence rate	1.87	Convergence rate	2.61
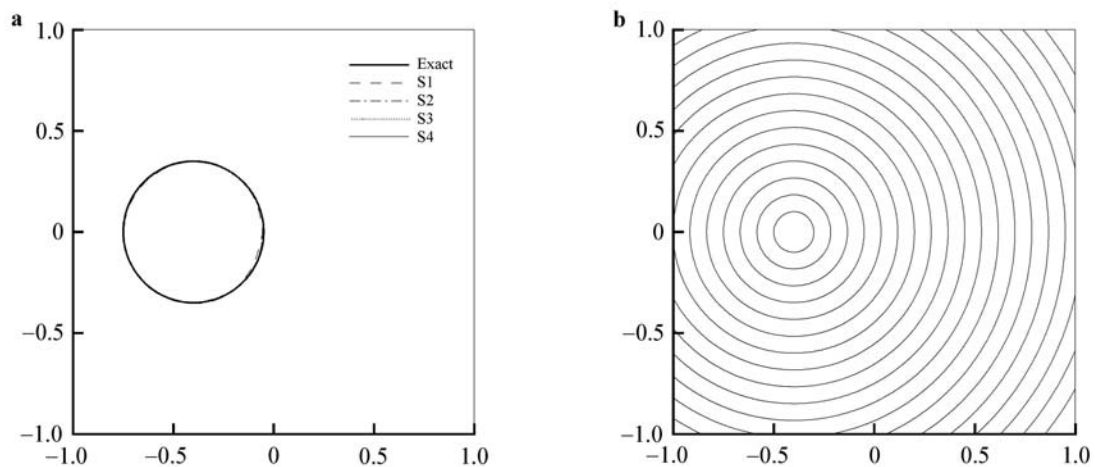
Fig. 4 Comparison of exact and numerical solutions on four grid sizes at time $t = 4.0$ of Problem 4.1. **a** Zero level set function; **b** Level set function (grid S4)

Finally, the non divergence-free velocity field case where $v_n = 0.1$ is examined. The final time is selected as 1.0 where the radius of circle is 0.45. The zero level set function of the exact and numerical solutions obtained from four grid sizes are presented in Fig. 5a. The figure shows that the differences of the interface position between the exact and numerical solutions are still very small. The signed distance function is also preserved during the simulation as depicted in Fig. 5b.
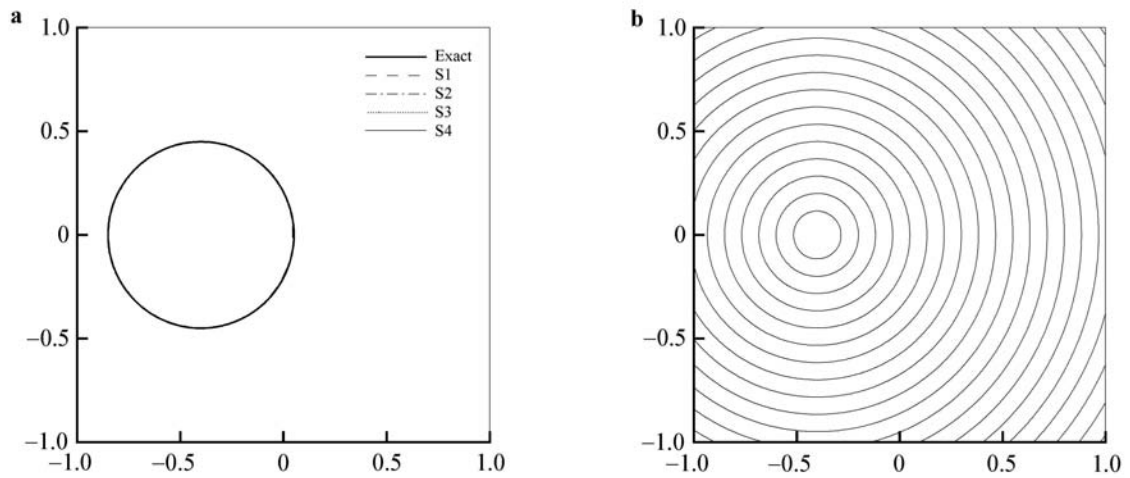
Fig. 5 Comparison of exact and numerical solutions on four grid sizes at time $t = 1.0$ of Problem 4.1 ($v_n = 0.1$). **a** Zero level set function; **b** Level set function (grid S4)

4.2 Rotation of a slotted disk

The second benchmark problem is a rotation of a slotted disk in a square domain of $\Omega = (0, 0) \times (1, 1)$ [21,22]. This example has an analytical solution so that the numerical solution can be compared. Initially, the slotted disk with a radius of 0.15 is centered at (0.5, 0.75) with a slot width of 0.05. The function ϕ_0 is defined as the signed distance function from the object. The slotted disk is rotated with the divergence-free velocity field defined by

$$V = [2\pi(y - 0.5), \; -2\pi(x - 0.5)]. \tag{19}$$

Although this problem involves only with the divergence-free velocity, but the computation is more severe than the first problem. The problem has sharp corners with the notch that tends to diffuse if the numerical dissipation is too large. To assess the convergence order of the proposed method, simulations are performed on uniform grids S1 to S4 again. Comparison between the analytical and numerical zero level set functions at the four different times of 0.25, 0.5, 0.75, and 1.0 are presented in Fig. 6. These figures show that the grid S1 is too coarse and the notch disappears after one rotation. However, the differences of the interface position between the analytical and numerical solutions decrease for grid S2, and are very small for grids S3 and S4. The values of the $\|L_{1,I}\|$ error norms and the rate of convergence are tabulated in Table 1. The convergence rate for this problem is less than second order of about 1.87 due to the presence of the sharp corners. The order for the solution accuracy of this problem is still closed to two because the slope limiter function is not applied to Eq. (16) to prevent oscillations along discontinuity of the zero level set function. Figures 7a and 7b show the

level set functions at $t = 1.0$ obtained from grids S4 and S5 in which the signed distance function is preserved during the simulation. The grid S5 (512×512) yields very sharp corners of the slotted disk similar to those of the exact solution.
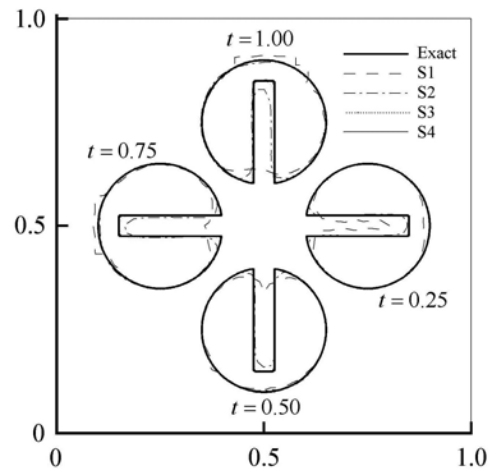

Fig. 6 Comparison of exact and numerical solutions on four grid sizes of Problem 4.2

The conservation of area is examined for grids S2 to S5 as shown in Fig. 8, where the area inside the zero level set is defined by $A(t) = \int_\Omega H(\phi_{\text{num}}) d\boldsymbol{x}$. This figure shows that the mass loss increases rapidly on grid size S2 because the grid size is not small enough. The mass conservative property is improved significantly as the grid is refined, such as for grid size S5 where the history line of mass conservative property is flat.
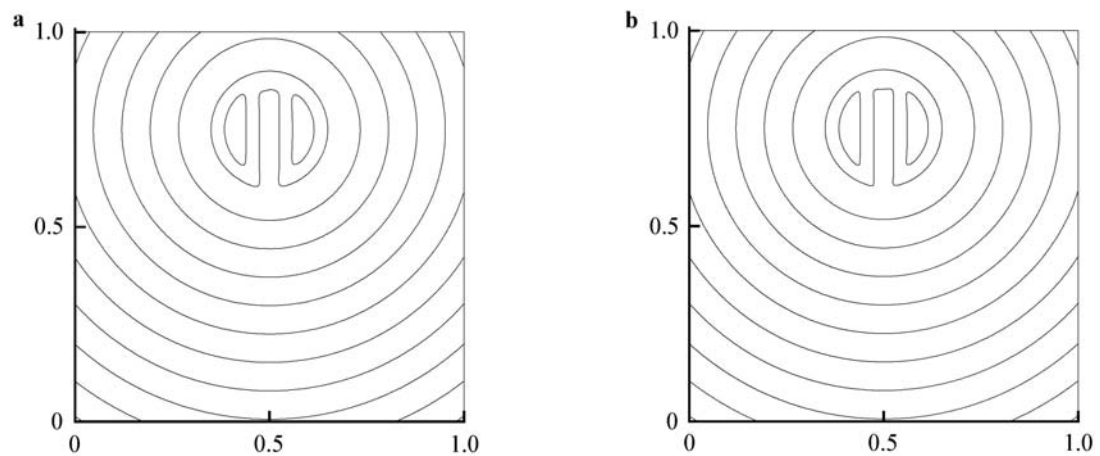
Fig. 7 Plot of level set function on fine grid sizes for Problem 4.2. **a** Grid S4; **b** Grid S5
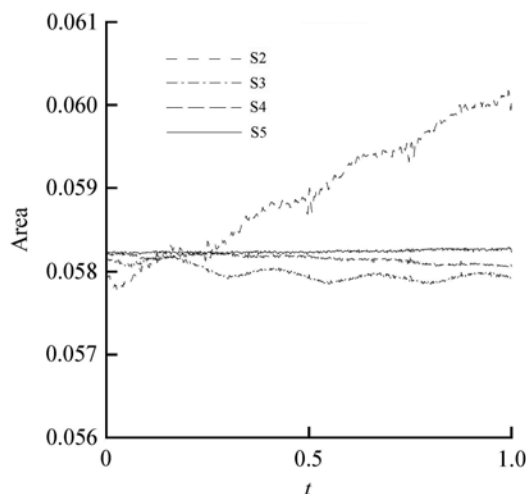
Fig. 8 Plot of area conservation of numerical solutions of Problem 4.2

4.3 Reversed vortex test

The third benchmark problem is a very complicated advection flow in a square domain of $\Omega = (0, 0) \times (1, 1)$ [9]. A circle with radius of 0.15 centered at (0.5, 0.75) is used as initial condition. The velocity field is defined by

$$V = [-\sin^2(\pi x)\sin(2\pi y), \ \sin^2(\pi y)\sin(2\pi x)]. \tag{20}$$

The problem is tested at the final time $T = 2.0$. The flow field is reversed at a half time of $t = T/2$ for which the exact solution at $t = 2.0$ must coincide with the initial condition. The given condition causes the flow to return to its initial state at time $t = T$ so that the quantitative error of the computed solution can be measured easily. The maximum distortion from the initial interface shape occurs at $t = T/2$. As the reversal period T becomes larger, the interface stretches further away from its initial circular shape. Comparisons of zero level set functions obtained from grids S1–S4 at $t = 0.25$, 0.5, 0.75, and 1.0 are presented in Figs. 9a–9d, respectively. These figures show that grids S1 and S2 are coarse because

the pinch off [9] appears during the evolution. The interface remains well resolved by using the refined grids S3 and S4. The comparison between exact and numerical solutions at time $t = 2.0$ is shown in Fig. 10. The differences of the interface position between the exact and numerical solutions are very small for grids S3 and S4.

To investigate the conservation of area property of the proposed numerical scheme, this problem is tested again on a very fine grid S5. The conservation of areas for grids S2 to S5 are examined as shown in Fig. 11. The mass loss increases rapidly for grid size S2 because the grid size is not small enough. The mass conservative property improves significantly as the grids are refined, such as for grids S4 and S5 where the history line of mass conservative property is flat. By comparing with the second benchmark problem, the conservative property of the proposed numerical scheme is stable and improved as compared with the one that consists of the discontinuous zero level set function. The values of the $\|L_{1,I}\|$ error norms and the rate of convergence are listed in Table 1. The convergence rate for this problem is second order of about 2.61.

Finally, this problem is tested again on grids S4 and S5 for a longer final time of $t = 4.0$ to investigate its robustness and to ensure that the proposed numerical scheme does not need the reinitialization in order to heal the distorted and stretched level set field for a long time simulation. The plots of the zero level set of both grids S4 and S5 are shown in Figs. 12a and 12b, respectively. There is no pinch off in these figures as compared to those presented in Ref. [9]. The numerical results are comparable with those reported by Ref. [23] where more complicated Lagrangian particle level set method is incorporated with frequently remeshing technique and reinitialization. This example suggests that the proposed numerical scheme offers advantages suitable for implementation in the commercial software, such as the second-order solution accuracy, conservative and simple implementation, low resources requirement and improved computational efficiency.
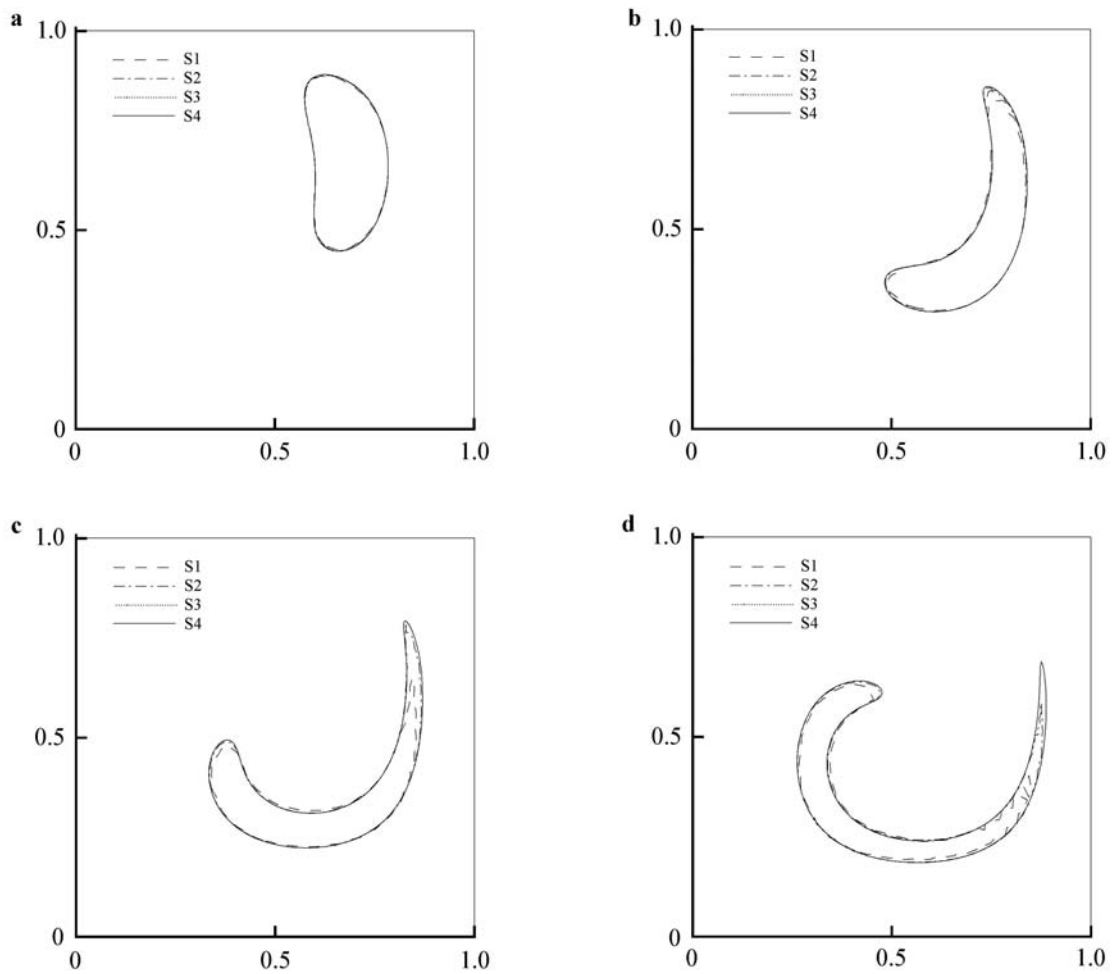
Fig. 9 Comparison of numerical solutions on four grid sizes of Problem 4.3. **a** $t = 0.25$; **b** $t = 0.50$; **c** $t = 0.75$; **d** $t = 1.0$
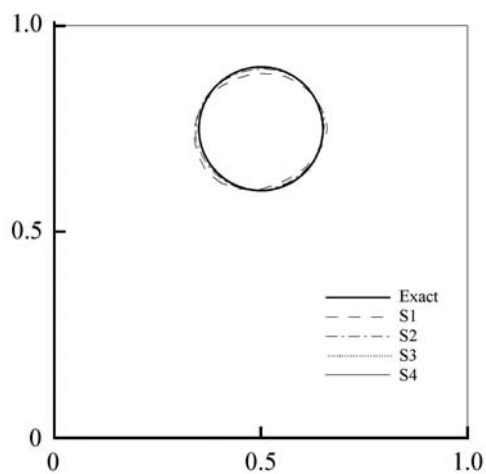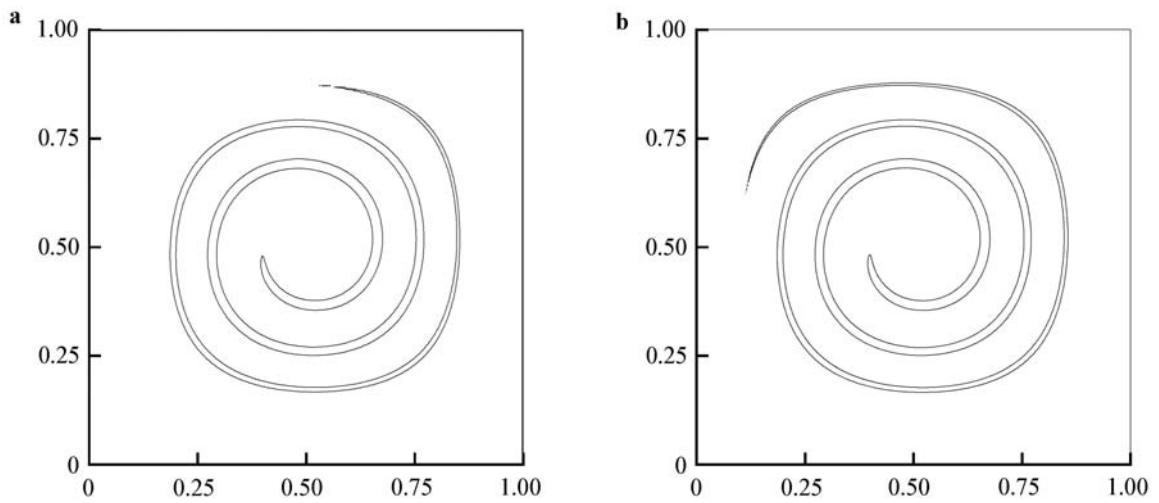

Fig. 10 Comparison of exact and numerical solutions at time $t = 2.0$ of Problem 4.3
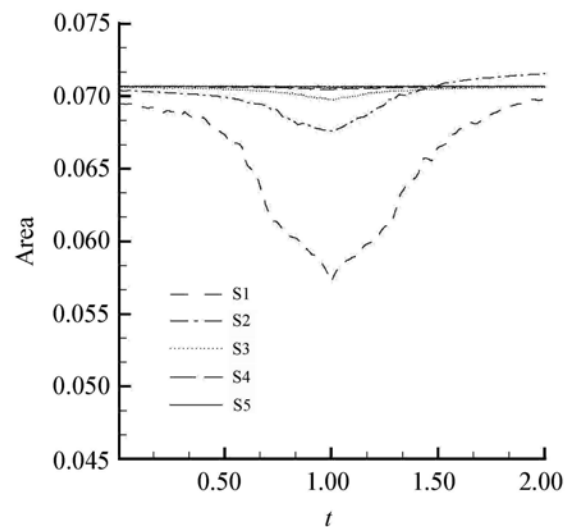
Fig. 11 Plot of area conservation of numerical solutions of Problem 4.3

Fig. 12 Plot of level set function on fine grid sizes at time $t = 4.0$ of Problem 4.3. **a** Grid S4; **b** Grid S5

4.4 Motion by mean curvature of a star shape

The fourth test case is used to examine the performance of the proposed method for calculating the curvature of a star shape [3], where the motion of simply-closed curve collapse with the speed proportional to the local curvature. This problem is tested by using the same domain size as described in the previous problems. The initial condition of the star shape is given by

$$\phi(x, y) = r - 0.2 \left[\cos \left(7 \tan \frac{y}{x} \right) + 2.5 \right], \tag{21}$$

where $r = \sqrt{x^2 + y^2}$ and the coefficient of curvature term b is set to 0.02.

The challenging task of this test case is to verify the Grayson's theorem [24] such that all simply closed curves eventually collapse to a round point. Due to the effect of the curvature, the initial star shape will deform into a round-shape. Numerical solutions are presented by using only grids S1 and S2 herein because the solutions from grids S3 and S4 are similar. The initial form of the star shape in 2D and 3D plots are shown in Figs. 13a and 13b, respectively. Figure 14a shows the zero level set functions obtained from grid S1 at $t = 0.25, 0.5, 0.75$, and 1.0, respectively, and Fig. 14b shows the similar solutions but are obtained from grid S2. These solutions are similar to those reported in Ref. [3]. The numerical solution at time $t = 1.0$ confirms that the Grayson's theorem is numerically verified.
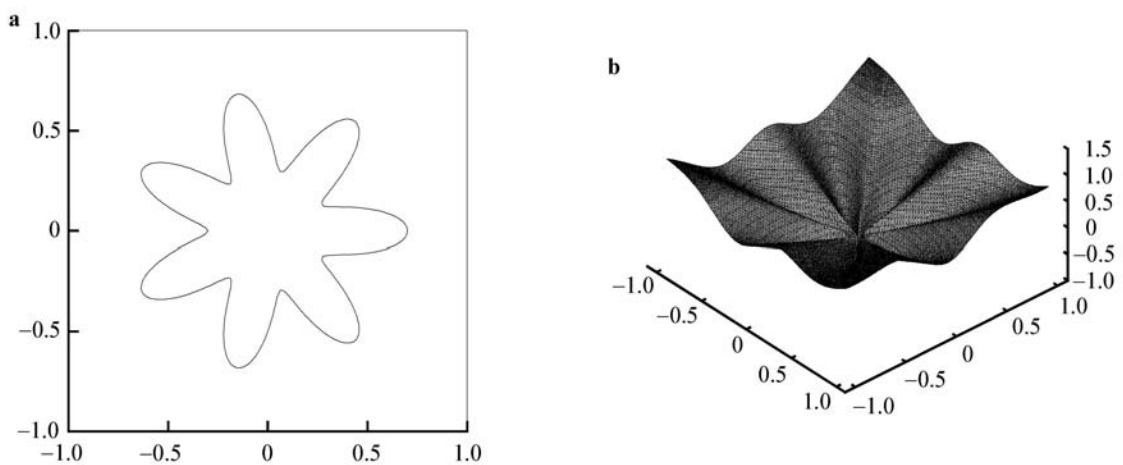
Fig. 13 Plots of initial condition of Problem 4.4. **a** 2D zero level set function; **b** 3D plot
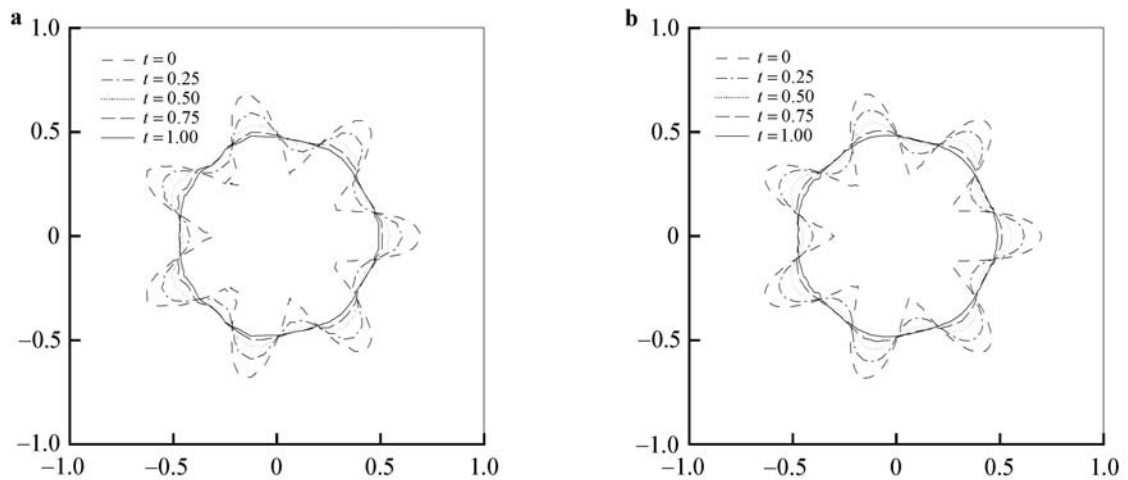
Fig. 14 Comparison of numerical solutions at four final times of Problem 4.4. **a** Grid S1; **b** Grid S2

4.5 Rayleigh–Taylor instability problem

The Rayleigh–Taylor instability problem is selected as the last example to evaluate the efficiency of the proposed scheme for simulating two-phase immiscible incompressible flow phenomena. The governing equations are [21]

$$\frac{\partial \rho(\phi)}{\partial t} + \boldsymbol{\nabla} V = 0, \tag{22}$$

$$\rho(\phi)\left(\frac{\partial V}{\partial t} + V \cdot \boldsymbol{\nabla} V\right) = -\boldsymbol{\nabla} p + \boldsymbol{\nabla}(2\mu D) - \sigma \kappa(\phi)\delta(\phi)\boldsymbol{\nabla}\phi, \tag{23}$$

where ρ and μ are the density and viscosity, respectively. These properties are constant in each fluid and can be written as

$$\rho(\phi) = \rho_1 + (\rho_2 - \rho_1)H(\phi), \tag{24}$$

$$\mu(\phi) = \mu_1 + (\mu_2 - \mu_1)H(\phi). \tag{25}$$

In the above equations, p is the pressure, D is the rate of deformation tensor, and $H(\phi)$ is a smeared out Heaviside function such as [9]

$$H(\phi) = \begin{cases} 0, & \phi < -\varepsilon, \\ \frac{1}{2}\left[1 + \frac{\phi}{\varepsilon} + \frac{1}{\pi}\sin\left(\frac{\pi\phi}{\varepsilon}\right)\right], & -\varepsilon \leq \phi \leq \varepsilon, \\ 1, & \phi > \varepsilon, \end{cases} \tag{26}$$

and the smoothed delta function is defined by

$$\delta(\phi) = \begin{cases} \frac{1}{2\varepsilon}\left[1 - \cos\left(\frac{\pi\phi}{\varepsilon}\right)\right], & -\varepsilon \leq \phi \leq \varepsilon, \\ 0, & \text{otherwise.} \end{cases} \tag{27}$$

The curvature of the interface, κ is expressed as

$$\kappa = \boldsymbol{\nabla} \cdot \left(\frac{\boldsymbol{\nabla}\phi}{|\boldsymbol{\nabla}\phi|}\right)\bigg|_{\phi=0}. \tag{28}$$
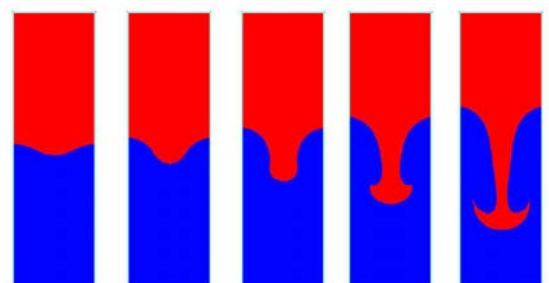
The characteristic-based split finite element method is applied to Eqs. (22) and (23) by following the same idea as

explained by Traivivatana et al. [25]. Finally, the hybrid finite element/finite volume solver is derived for solving the two-phase immiscible incompressible flow problem. The Rayleigh–Taylor instability problem is associated with the acceleration of a heavy fluid into a light one under the action of a gravitational field [26]. The domain is defined by $\Omega = (0, 1) \times (0, 4)$, and fluid properties are given by

$$\rho_1 = 0.17\,\text{kg/m}^3, \qquad \mu_1 = 1.6 \times 10^{-5}\,\text{N} \cdot \text{s/m}^2, \tag{29}$$

$$\rho_2 = 1.2\,\text{kg/m}^3, \qquad \mu_2 = 3.0 \times 10^{-3}\,\text{N} \cdot \text{s/m}^2, \tag{30}$$

where the coefficient of surface tension and gravity is $0.015\,\text{N/m}$ and $9.87\,\text{m/s}^2$, respectively. This problem is tested on triangular mesh with 40×160 nodes. The simulation is terminated at the time of $t = 1.0$. Snapshots of typical results shown by Fig. 15 explain development of the instability as the heavy fluid penetrates through the light fluid to form the mushroom shape. The effect of surface tension is clearly seen from the figure for which the growth rate of the Rayleigh–Taylor instability decreases to make the interface smoother and more compact.

Fig. 15 Snapshots of results at difference time steps for Problem 4.5

5 Conclusions

The paper presents an explicit finite volume element method

for solving the characteristic level set equation in a two-dimensional domain. The theoretical formulation of the characteristic level set equation developed by using the characteristic-based scheme was explained in details. The finite volume method was used to derive the discretized equations for the spatial domain. Gradients at cell faces for determining the curvature term are determined by applying the weighted-residual finite element technique. Four numerical examples were used to evaluate the performance and to determine the order of accuracy of the proposed method. These examples have shown that the method provides converged solution with improved accuracy as the grid is refined, and the conservative property is preserved without reinitialization in order to heal the distorted and stretched level set field. Finally, the proposed level set method was coupled with the Navier–Stokes equations for analyzing the two-phase immiscible incompressible flow with surface tension. The hybrid finite element/finite volume method was derived and tested by solving the Rayleigh–Taylor instability problem.

References

1 Osher, S., Sethian, J.A.: Fronts propagating with curvature-dependent speed: algorithms based on Hamilton-Jacobi formulations. J. Comput. Phys. **79**(1), 12–49 (1988)

2 Scardovelli, R., Zaleski, S.: Direct numerical simulation of free-surface and interfacial flow. Annu. Rev. Fluid Mech. **31**, 567–603 (1999)

3 Osher, S., Fedkiw, R.: Level Set Methods and Dynamic Implicit Surfaces. Springer, New York (2003)

4 Sethian, J.A.: Level Set Methods and Fast Marching Methods. Cambridge University Press, Cambridge (1999)

5 Duflot, M.: A study of the representation of cracks with level sets. Int. J. Num. Meth. Enrgr. **70**(11), 1261–1302 (2007)

6 Mei, Y.L., Wang X.M.: A level set method for structural topology optimization with multi-constraints and multi-materials. Acta Mech. Sin. **20**(5), 507–518 (2004)

7 Zhang, X., Zhao, N.: A robust algorithm for moving interface of multi-material fluids based on Riemann solutions. Acta Mech. Sin. **22**(2), 509–519 (2006)

8 Sethian, J.A., Smereka, P.: Level set methods for fluid interfaces. Annu. Rev. Fluid Mech. **35**, 341–372 (2003)

9 Olsson, E., Kreiss, G.: A conservative level set method for two phase flow. J. Comput. Phys. **210**(1), 225–246 (2005)

10 Fedkiw, R.P.: Coupling an Eulerian fluid calculation to a Lagrangian solid calculation with the ghost fluid method. J. Comput. Phys. **175**(1), 200–224 (2002)

11 Huang, J., Zhang, H.: Level set method for numerical simulation of a cavitation bubble, its growth, collapse and rebound near a rigid wall. Acta Mech. Sin. **23**(6), 645–653 (2007)

12 Tanguy, S., Menard, T., Berlemont, A.: A level set method for vaporizing two-phase flows. J. Comput. Phys. **221**(2), 837–853 (2007)

13 Barth, T.J.: Numerical schemes for the Hamilton-Jacobi and level set equations on triangulated domains. J. Comput. Phys. **145**(1), 1-40 (1998)

14 Frolkovic P, Mikula K.: High-resolution flux-based level set method. SIAM J. Sci. Comput. **29**(2), 579–597 (2007)

15 Frolkovic, P., Mikula, K.: Flux-based level set method: a finite volume method for evolving interfaces. Appl. Numer. Math. **57**(4), 436–454 (2007)

16 Aboubacar, M., Webster, M.F.: Development of an optimal hybrid finite volume/element method for viscoelastic flows. Int. J. Num. Meth. Fluids **41**(11), 1147–1172 (2003)

17 Chandio, M.S., Sujatha, K.S., Webster, M.F.: Consistent hybrid finite volume/element formulations: model and complex viscoelastic flows. Int. J. Num. Meth. Fluids **45**(9), 945–971 (2004)

18 Zienkiewicz, O.C., Codina, R.: A general algorithm for compressible and incompressible flow—part I. the split, characteristic-based scheme. Int. J. Num. Meth. Fluids **20**(8-9), 869–885 (1995)

19 Zienkiewicz, O.C., Taylor, R.L.: The Finite Element Method for Solid and Structural Mechanics. (6th edn.) Butterworth-Heinemann, Burlington (2005)

20 Phongthanapanich, S., Dechaumphai, P.: Finite volume element method for analysis of unsteady reaction-diffusion problems. Acta Mech. Sin. **25**(4), 481–489 (2009)

21 Sussman, M., Fatemi, E.: An efficient, interface-preserving level set redistancing algorithm and its application to interfacial incompressible fluid flow. SIAM J. Sci. Comput. **20**(4), 1165–1191 (1999)

22 Zalesak, S.T.: Fully multidimensional flux-corrected transport algorithms for fluids. J. Comput. Phys. **31**(3), 335–362 (1979)

23 Hieber, S.E., Koumoutsakos P.: A Lagrangian particle level set method. J. Comput. Phys. **210**(1), 342–367 (2005)

24 Grayson, M.A.: The heat equation shrinks embedded plane curves to round points. J. Differential Geometry **26**(2), 285–314 (1987)

25 Traivivatana, S., Boonmarlert, P., Theeraek, P., et al.: Combined adaptive meshing technique and characteristic-based split algorithm for viscous incompressible flow analysis. Appl. Math. Mech. **28**(9), 1163–1172 (2007)

26 Puckett, E.G., Almgren, A.S., Bell, J.B., et al.: A high-order projection method for tracking fluid interfaces in variable density incompressible flows. J. Comput. Phys. **130**(2), 269–282 (1997)